Effect of salinity, pressure and temperature on the solubility of smithsonite ($ZnCO_3$) and Zn complexation in crustal and upper mantle hydrothermal fluids

Stefan Farsang[1*], Marion Louvel[2], Angelika D. Rosa[3], Monica Amboage[4], Simone Anzellini[4], Remo N. Widmer[5], and Simon A. T. Redfern[6#]

[1]Department of Earth Sciences, University of Cambridge, Downing Street, Cambridge, CB2 3EQ, United Kingdom (*sf571@cam.ac.uk)

[2]Institut für Mineralogie, WWU Münster, 48149 Münster, Germany

[3]European Synchrotron Radiation Facility, 71 Avenue des Martyrs, 38000 Grenoble, France

[4]Diamond Light Source Ltd., Harwell Science and Innovation Campus, Didcot, OX11 0DE, United Kingdom

[5]Empa, Swiss Federal Laboratories for Materials Science and Technology, Laboratory for Mechanics of Materials and Nanostructures, Feuerwerkerstrasse 39, Thun, 3602, Switzerland

[6]Asian School of the Environment, Nanyang Technological University, 50 Nanyang Avenue, Singapore, 639798, Singapore ([#]simon.redfern@ntu.edu.sg)

Abstract

Modelling the reservoirs and fluxes of Zn in Earth's crust and mantle requires data on the solubility of its mineral hosts and ores in coexisting fluids, as well as on the complexation of Zn in these fluids as a function of fluid composition, pressure, and temperature. However, due to experimental challenges, the availability of such data is limited to pressures below 1 GPa, which are only representative of upper crust conditions.

Here, we report the effects of salinity (0-4.5 m total Cl), pressure (0.5-6 GPa) and temperature (25-400 ˚C) on the solubility of smithsonite ($ZnCO_3$) and speciation of Zn in aqueous fluids. Solubilities at mineral-fluid equilibria and Zn speciation in the coexisting aqueous fluids were determined *in situ* at high pressure-temperature (*P-T*) conditions by synchrotron X-ray fluorescence (XRF) and X-ray absorption spectroscopy (XAS) using resistively heated diamond anvil cells (RH-DAC). The solubility of smithsonite increases with salinity, pressure, and temperature. In agreement with previous studies, conducted at lower pressures (below 1 GPa), we observed a gradual transition from octahedral hydrated $[Zn(H_2O)_6]^{2+}$ to tetrahedral hydrated and chlorinated $[Zn(H_2O)_{4-n}Cl_n]^{2-n}$ (n = 1-4) complexes with increasing salinity and temperature. Our results suggest that these tetrahedral complexes remain stable under the conditions relevant to cold slab dehydration. This change of coordination further enhances the solubility of smithsonite in Cl-rich fluids and provides a likely mechanism for the efficient uptake of Zn by slab-derived fluids.

Keywords

Zinc speciation, smithsonite, solubility, subduction zone fluids, deep Earth, high pressure, high temperature, salinity, synchrotron XRF, XAS, DAC.

Introduction

In industrial applications, zinc (Zn) is the fourth most consumed metal in the world (USGS 2020), a critical component of alloys and an efficient anticorrosive. There is thus a significant commercial interest in understanding its geological occurrence and how its global geochemical cycle may relate to its concentration in different environments.

Many Zn ore deposits are hydrothermal in origin, with sphalerite (ZnS) being the most important and widespread ore mineral of Zn, followed by its prevalent weathering product, smithsonite ($ZnCO_3$). Smithsonite is expected to remain stable under the increasing *P*-*T* conditions of subducting slabs and could thus play a significant role in the cycling of Zn. Its stability is mainly constrained by its thermal decomposition to ZnO and CO_2 that takes place around 400 ˚C in air at ambient pressure (Preis et al. 2000; Farsang et al. 2021). At high pressures and temperatures, only data from experiments using CO_2 as a pressure medium are available (Haselton and Goldsmith 1987). The stability field of smithsonite increases rapidly with CO_2 pressure: at 0.3 GPa its breakdown is observed above 447 ˚C, while at 2 GPa smithsonite remains stable up to 875 ˚C (Haselton and Goldsmith 1987). Although the stability of smithsonite has been confirmed to pressures of at least 50 GPa at ambient temperatures (Gao et al. 2014), simultaneous high-pressure high-temperature studies above 2 GPa are, to the best of our knowledge, lacking. Furthermore, the stability of smithsonite in aqueous fluids also remains unknown.

The Zn isotopic system has been suggested as a recorder of the composition and oxidation state of fluids released to the mantle wedge or to trace the contribution of slab material to the mantle chemistry (Liu et al. 2016; Pons et al. 2016). Pons et al. (2016), for instance, attributed the decrease of δ^{66}Zn associated with decreasing sulphur contents in subducted Alpine serpentinites to the release of oxidized sulfate-rich fluids with heavy δ^{66}Zn isotopic signatures, based on theoretical calculations of δ^{66}Zn for Zn chloride and sulphate aqueous species (Fujii et al. 2014). Furthermore, Liu et al. (2016) ascribed the heavy δ^{66}Zn of continental basalts from eastern China (0.30-0.63‰, compared to 0.28‰ for the average mantle) to the low degree melting of carbonated peridotites, thus suggesting the deep recycling of isotopically heavy marine carbonates (0.91‰) in the mantle beneath eastern China.

Further development of Zn as a potential tracer of subduction zone processes requires a better understanding of Zn mobilization, transport, and recycling at subduction zones. In particular, it is critical to better quantify its speciation and solubility in Cl-rich fluids, which are the dominant mobile phases formed during slab dehydration (*e.g.*, Scambelluri and Philippot 2001; Weiss et al. 2015). Zn complexation has previously been inferred from solubility experiments (Ruaya and Seward 1986; Bourcier and Barnes 1987; Plyasunov and Ivanov 1991; Akinfiev and Tagirov 2014). The studies of Ruaya and Seward (1986) and Akinfiev and Tagirov (2014) found $[ZnCl_4]^{2-}$ to be the most stable complex at high total Cl^- concentrations (Cl_{tot}) and high temperatures, while both $[ZnCl_2]^0$ and $[ZnCl_4]^{2-}$ (Plyasunov and Ivanov, 1991) as well as $[ZnCl_3]^-$ (Bourcier and Barnes, 1987) have been reported as predominant species under these conditions. Mei et al. (2015) recently pointed out the discrepancy for formation constants of Zn-Cl species and the difference in speciation models implied by these studies.

Compared with such earlier solubility experiments, X-ray absorption spectroscopy (XAS), including X-ray absorption near-edge structure (XANES) and extended X-ray absorption fine structure (EXAFS), serves as an excellent tool to investigate the structure of specific target elements in aqueous solutions at the molecular level. XAS experiments, conducted on Zn-systems in pure H_2O and Cl-rich solutions from room temperature to high *P*-*T* conditions, revealed that Zn aqueous speciation evolves from being dominated by the octahedral hydrated ion $[Zn(H_2O)_6]^{2+}$ to the tetrahedral chloride complex $[ZnCl_4]^{2-}$ with increasing salinity (Mayanovic et al. 1999; Bassett et al. 2000; Liu et al. 2007). While at 25 ˚C, $[ZnCl_4]^{2-}$ becomes the dominant species for Cl concentration in excess of 1 m, in ~1 m Cl solutions, intermediate species $[ZnCl(H_2O)_3]^+$ and $ZnCl_2(H_2O)_2$ were reported to form at 25 ˚C and persist up to 660 ˚C and 0.8 GPa. Recent combined XAS and *ab initio* molecular dynamics (MD) simulations by Mei et al. (2015) also reported the same influence of increased salinity and temperature on the transition from octahedral hydrated species to tetrahedral chloride complexes. In detail, their XAS analysis demonstrated that higher Cl concentrations enable the formation of Zn-Cl tetrahedral complexes at lower temperatures (400 ˚C for 0.1 Cl to 100 ˚C for 3.7 m Cl) and further suggested a gradual evolution with increasing salinity, where $ZnCl_2(H_2O)_2$ becomes the dominant high-temperature species in the Cl-poor end-member (0.1 m Cl) while $[ZnCl_4]^{2-}$ dominates in the Cl-rich fluids (3.7 m Cl).

The formation of tetrahedral Zn-Cl complexes with increasing temperature and salinity has been suggested to account for the enhanced solubility of sphalerite (ZnS), zincite (ZnO), and smithsonite under shallow hydrothermal conditions (Mei et al., 2015). Amongst these different Zn-bearing phases, the stability of smithsonite at high pressures and high temperatures makes it a likely candidate host to transport Zn into the mantle at subduction zones and further control its release to the slab-mantle wedge interface. Published solubility data on smithsonite have been compiled by Clever et al. (1992). An internally consistent set of thermodynamic properties of smithsonite, based on its solubility and thermal decomposition, has been suggested by Preis et al. (2000). They investigated the solubility of smithsonite in 1 m $NaClO_4$ aqueous solution as a function of temperature from 15 to 65 ˚C and as a function of ionic strength in 1, 2, and 3 m $NaClO_4$ aqueous solutions at 25 ˚C and found a solubility decrease with temperature and a solubility increase with salinity up to 1 m $NaClO_4$, followed by a decrease above this value (Preis et al. 2000). The effects of salinity, pressure, and temperature on Zn speciation and smithsonite solubility however remain unknown at slab dehydration conditions (P > 1 GPa and T > 300 ˚C).

Here, we report results from in-situ XRF and XAS experiments on fluid-smithsonite equilibria in the diamond anvil cell (DAC). We have investigated the solubility of smithsonite in water, 1 and 4.5 m NaCl aqueous solutions up to 6 GPa and 400 ˚C. We have also measured Zn complexation in aqueous solutions with 0.2, 1, and 4 m Cl_{tot} and corresponding Cl:Zn ratios of 2:1, 10:1, and 40:1 up to 2 GPa and 400 ˚C.

Materials and experimental methods

Starting materials

A natural smithsonite sample provided by the Natural History Museum, London with specimen number BM.1929,1637 originating from Kopje number 1, Kabwe (Broken Hill), Kabwe, Central Province, Zambia was used for the solubility experiments. Prior to the solubility experiments, the specimen was characterized by electron probe microanalysis (EPMA), X-ray diffraction (XRD), and Raman spectroscopy. The calculated chemical formula based on EPMA is $Zn_{0.97}Mg_{0.02}Ca_{0.01}CO_3$, the unit cell parameters (in the hexagonal setting) were determined from X-ray powder diffraction as a = 4.65545(9) Å and c = 15.0475(4) Å, and the Raman spectrum has been reported in Farsang et al. (2021).

The compositions of the different fluids used are reported in Table 1. Experiments in pure water were conducted using Milli-Q water. The NaCl aqueous solutions of 1 and 4.5 m concentration were prepared using high purity NaCl (>99.999%, Sigma Aldrich).

Reference solutions with total Zn concentrations of 0.02 m, 0.1 m, and 0.2 m were prepared using $ZnCl_2$ (99.999%, Sigma Aldrich). Due to the hygroscopic nature of $ZnCl_2$, the precise Zn concentration of solutions was further determined by inductively coupled plasma mass spectroscopy (ICPMS).

<table>
<tr><td colspan="4">Dissolution experiments in the $ZnCO_3$(s)-NaCl-H_2O system</td></tr>
<tr><td colspan="2">Experiment number</td><td colspan="2">Composition</td></tr>
<tr><td colspan="2">1</td><td colspan="2">$ZnCO_3$(s) in double distilled and deionized water</td></tr>
<tr><td colspan="2">2</td><td colspan="2">$ZnCO_3$(s) in 1 m NaCl(aq)</td></tr>
<tr><td colspan="2">3</td><td colspan="2">$ZnCO_3$(s) in 4.5 m NaCl(aq)</td></tr>
<tr><td colspan="4">Speciation experiments in the $ZnCl_2$-NaCl-H_2O system</td></tr>
<tr><td>Solution number</td><td>Composition</td><td>Total Cl concentration</td><td>Cl:Zn ratio</td></tr>
<tr><td>1</td><td>0.1 m $ZnCl_2$(aq)</td><td>0.2 m</td><td>2:1</td></tr>
<tr><td>2</td><td>0.1 m $ZnCl_2$(aq) + 0.8 m NaCl(aq)</td><td>1 m</td><td>10:1</td></tr>
<tr><td>3</td><td>0.1 m $ZnCl_2$(aq) + 3.8 m NaCl(aq)</td><td>4 m</td><td>40:1</td></tr>
</table>

Table 1. Dissolution and speciation experiments performed in the present study.

Speciation experiments were performed on three Zn-bearing solutions with total Cl concentrations of 0.2 m, 1 m, and 4 m, prepared using $ZnCl_2$ (99.999%, Sigma Aldrich) and NaCl (99.999%, Sigma Aldrich). The compositions of solutions reflect the wide range of salinity found in natural fluid inclusions (*e.g.*, Scambelluri and Philippot 2001; Weiss et al. 2015) and are reported in Table 1.

Smithsonite solubility by in situ synchrotron X-ray fluorescence spectroscopy

Smithsonite solubility experiments in pure water and saline solutions were carried out at the X-ray absorption beamline BM23 of the European Synchrotron Radiation Facility in Grenoble, France (Mathon et al. 2015) (Figure 1). The operating conditions of the storage ring were 6 GeV and 180-200 mA in top-up mode.

All experiments were conducted using membrane-type diamond anvil cells (Letoullec et al. 1988) equipped with type Ia single crystal diamond anvils with culet diameters of 500 μm. A partially perforated diamond anvil with a remaining thickness of ~150 um facing the XRF detector was employed to minimize the absorption of the fluorescence signal from the diamond. The diamonds were cleaned before use in H_2SO_4 for several hours. Rhenium gaskets were employed, pre-indented from an initial thickness of 200 μm to ~80 μm, then laser drilled with a 200 μm diameter hole, and lined with a 25 μm gold layer to prevent Re dissolution in the high *P*-*T* fluid.

Smithsonite crystals of known volume (~20 x 20 x 20 μm) were loaded in the sample chamber (~1.4 x 10^6 μm^3) together with the aqueous solution. Pressure was remotely controlled and increased stepwise to the target pressure. During cold compression and heating we used the diffraction signal of gold and the thermal equation of state reported by Fei et al. (2007) to determine the pressure. The incident X-ray beam energy for X-ray diffraction was 15 keV. Diffraction data were recorded using a 165 mm diameter MarCCD XRD detector positioned on the downstream side of the DAC (Figure 1). A CeO_2 standard was used to calibrate the distance, detector tilt, and rotation parameter. The 2D diffraction images were integrated using Dioptas software (Prescher and Prakapenka 2015). Uncertainties in pressure determination are estimated to be approximately 5 % of the pressure values at all investigated temperatures.

The DAC was heated resistively using an external heating device developed at the European Synchrotron Radiation Facility. In this setup, the DAC and its heater were enclosed in a vacuum chamber equipped with Mylar windows that permit the transmission of X-rays. A high vacuum of up to 10^{-6} bars ensured a homogenous heating during the long duration of the experiments and prevents the oxidation of the diamonds and heater. The setup further allows for a fine and remote control of the pressure and temperature (Dewaele et al. 2018). For the latter, a K-type thermocouple is positioned close to the heater. A second thermocouple was placed in contact with one of the diamonds to monitor the sample temperature. Uncertainties in temperature determination are estimated to be ±2 ˚C.

X-ray fluorescence measurements at the BM23 beamline were conducted in back-scattered geometry. A fixed-exit double crystal monochromator equipped with two silicon (111) crystals was used to tune the X-ray beam energy to 11.0 keV (using the Au L_3 (11.9 keV) fluorescence line as a reference). The incoming X-ray beam was focused to a spot size of 3.6×5 ($h \times w$) μm^2 using a pair of Kirkpatrick-Baez (KB) mirrors coated with Pt and inclined to 4 mrad for harmonic rejection. The intensity of the beam before and after the sample was measured using two ion chambers filled with appropriated proportion of absorbing gas. The DAC was mounted on a hexapod motor system micrometre precision XYZ translation stage (Mathon et al. 2015). The DAC was aligned at a permanent angle of 17˚ with respect to the incoming X-ray beam, similar to the XRF detector and microscope. This geometry ensured that the full aperture of the diamond perforation was oriented towards the fluorescence detector.

The emitted fluorescence signal from the sample was collected using a HITACHI Vortex Si drift diode detector with a 40 mm^2 active area and a sensitive layer thickness of 1 mm. The detector was equipped with XOS polycapillary focusing optics, which allows the extraction of emitted fluorescence signal from a small sample area of 50×50 (h×w) μm^2, eliminating significantly the Compton scattering and diffused scattering from the sample environment (Wilke et al. 2010). The use of polycapillary increases drastically the signal-to-noise ratio at the expense of a reduced flux of emitted photons reaching the detector. The polycapillary half lens was repositioned onto the X-ray beam focus before every XRF acquisition by scanning the XRF detector horizontally and vertically. For this operation, the X-ray beam was placed onto the Re gasket and the intensity of the Re Lα (8.7 keV) fluorescence line was monitored during the scan. A microscope mounted on the back of the DAC was used to visualize the sample and to reposition it in the X-ray focal plane for XRF and XRD detection, respectively.

For each run, the sample was initially pressurized to ~2 GPa and then heated up to 300 ˚C (Figure 2). The pressure was then increased to ~6 GPa in pressure increments of ~1-2 GPa. Finally, the temperature was increased to 400 ˚C. Generally, two XRF spectra were collected at each high *P*-*T* step approximately 30 and 60 minutes after reaching the target *P*-*T*, each for 10 minutes. The intensity of the incoming beam (I_0) was measured immediately before and after each sample XRF collection in order to correct for intensity fluctuations of the incoming beam.

XRF spectra were analysed using PeakFit software. For each XRF spectrum, the X-ray photon background was subtracted and the area under the characteristic XRF bands was determined by least squares fitting to Voigt profiles. Once corrected for I_0 fluctuations, Re Lα contribution to the Zn Kα line (see below), and density effects induced by increasing pressure and temperature, concentrations of Zn are proportional to the area of the Zn Kα (8.6 keV) fluorescence lines, determined from the peak fitting and our fluorescence calibrations. The intensity of the Zn Kα fluorescence line was calibrated for the experimental setup using $ZnCl_2$ reference solutions with total Zn concentrations of 0.02 m, 0.1 m, and 0.2 m (Figure S1). Calibration and solubility measurements were conducted using the same experimental geometry (i.e., same beam optical path, constant distance between the sample and fluorescence detector, DAC centred on the X-ray focal point). The possibility of fluorescence from the Zn solid phase was ruled out by 1) placing the smithsonite crystal at the edge of the sample chamber, 2) scanning the XRF detector through the sample chamber in directions perpendicular to the incoming beam to find the position of crystal, 3) positioning the X-ray beam at a point in the fluid at least 50 μm distant from both the crystal and gasket. The fluorescence signal of the fluid (i.e., areas away from the crystal) was uniform, confirming fluid homogeneity as well as the absence of any contribution from the solid. Despite the very short beam path within the diamond cell, with only small distances (of the order of 10^{-5} m) involved, none the less we anticipate that some of the XRF signal is absorbed by the sample fluid itself. While absorption of 8.6 keV X-rays by 0.2 m $ZnCl_2(aq)$, H_2O, and 1 m NaCl(aq) is of very similar magnitude (8, 6 and 9%, respectively) over the interaction length corresponding to the sample chamber thickness, absorption by 4 m NaCl(aq) is 16%, i.e. twice as large as that of the most concentrated reference solution. Consequently, we anticipate that Zn solubility values in the 4 m NaCl(aq) sample are likely underestimated.

Typical uncertainties in the calculated Zn concentration at high *P*-*T* conditions are less than 30% of the measured values. Due to the overlap of the Zn Kα (8.6 keV) and the Re Lα (8.7 keV) fluorescence lines, the potential contribution of dissolved Re (gasket) in NaCl solutions to the Zn signal was tested by conducting a blank experiment (*i.e.*, no smithsonite crystal) following the same *P*-*T* path. The Re Lα peak in the Zn-free 1m NaCl solution was found to be weak and constant across the experimental conditions, thus further validating our Zn quantitative measurements in the DAC (Figure S2).

Zn speciation by in situ synchrotron X-ray absorption spectroscopy

The effect of increasing pressure, temperature, and salinity on Zn aqueous speciation was investigated *in situ* by XAS at the I20 energy dispersive (EDE) beamline at the Diamond Light Source Ltd. in Didcot, United Kingdom (Diaz-Moreno et al. 2018) (Figure 1c and d). The operating conditions of the storage ring were 3 GeV and 300 mA.

All experiments were conducted using a new hydrothermal diamond anvil cell (HXD95) designed for large-angle ($\theta = 95^{\circ}$) XRD measurements (Louvel et al. 2020). Here, the HXD95 was equipped with type Ia Boehler-Almax diamond anvils with culet diameter of 300 μm. The diamond anvil facing the detector was partially perforated to a thickness of ~150 μm in order to minimize the absorption of the X-ray beam and emitted photons at the low energy of the Zn K-edge. Zn-bearing solutions (Table 1) were loaded in 220 μm thick Au-lined (99.9%, Sigma Aldrich) Re gasket with a 200 μm diameter hole, together with a chip of zircon used as pressure calibrant. This geometry enables optimal XAS measurements with a maximum angular opening of 30-40 °.

The HXD95 was internally heated using a resistive heater comprising a Mo wire wound around the WC seats that support the diamond anvils. Temperature was increased using a remotely controlled DC power supply and monitored using two K-type thermocouples attached to the surface of both diamonds, as close as possible to the sample chamber. Uncertainties in temperature determination are estimated to be ±2 °C (Louvel et al. 2013).

The pressure inside the HXD95 was transmitted to the sample by tightening a set of three screws and monitored using the pressure and temperature-induced shifts of the $\nu_3(SiO_4)$ Raman band of zircon (Schmidt et al. 2013). A Horiba iHR320 Raman spectrometer with a 532 nm laser delivered via a superhead setup positioned at 90˚ from the incident beam was used to visualize the sample chamber and collect the Raman spectrum of the pressure sensor. The DAC was rotated by 90˚ for Raman measurements. Uncertainties in pressure determination are estimated to be 5 % of the pressure values.

XAS measurements were carried out in fluorescence geometry. A monochromatic beam was obtained by scanning a narrow horizontal slit through the beamline energy dispersed polychromatic beam. Spectra were collected across the Zn K-edge (9.659 keV) over an energy range of 9.625 – 10.015 keV. The energy was calibrated with a Zn foil measured in transmission mode with I_0 and I_t OKEN ion chambers. The incoming X-ray beam was focused to a spot size of 30×30 (h×w) μm^2 at the sample.

The HXD95 was mounted on a high-precision *XYZθ* remote-controlled rotating stage. It was placed with a permanent angle of 0˚ in respect to the incoming X-ray beam in the horizontal plane. The emitted fluorescence signal from the sample was collected using a Vortex-ME4 four-element Si drift detector with a 170 mm^2 active area and sensitive layer thickness of 0.35 mm, which was positioned at 20˚ from the incoming beam at the near side of the DAC.

For each experimental run, the sample was initially pressurized to ~0.5 GPa and spectra recorded at ambient temperature. Then, the sample was heated to the temperature of interest in ~100 ˚C increments (200 ˚C, 300 ˚C, or 400 ˚C) (Figure 2). Pressure was monitored at each temperature step, before and after XAS acquisition. At each *P*-*T* condition, XAS spectra were collected at two to three different angles (±5° from the optimal position) in order to eradicate any glitches resulting from diffraction from the diamond. At each angle, 20 spectra were collected for 120 s each.

X-ray absorption spectroscopy spectra analysis

The structural environment of Zn in high *P*-*T* fluids was determined using the Athena and Artemis packages, based on the IFEFFIT program (Ravel and Newville 2005). Averaged XAS spectra were first normalized to the absorption edge height and the spline background was removed using the automatic background subtraction routine AUTOBK implemented in the Athena software. The absorption edge E_0 was determined based on the maximum of the absorption edge first derivative.

X-ray absorption near edge structure (XANES) spectra collected at the Zn K-edge contain important information about the geometry of the aqueous species: especially a shift of E_0 from higher to lower energy is associated to the octahedral to tetrahedral transition (Liu et al. 2007; Mei et al. 2015; Etschmann et al. 2019). Linear combination fitting (LCF) of XANES spectra was hence also performed using the Athena software to retrieve the fractions of octahedral and tetrahedral Zn^{2+} complexes at each P-T-Cl_{tot} condition. The fitting was carried out on the normalized μ(E) spectra using two reference spectra that represent octahedral $Zn(H_2O)_6$ and tetrahedral $ZnCl_4$ endmembers. The relative proportions of the two components were allowed to vary from 0 to 1 and their sum was fixed to be 1.

Extended X-ray absorption fine structure (EXAFS) spectra carry additional information about Zn structural environments, including the number of neighbouring atoms in the first coordination shell and their distance to Zn central atom. EXAFS oscillations and their Fourier Transform over the 2.5-8 Å^{-1} range were fitted to the

EXAFS equation using the ARTEMIS software (Ravel and Newville 2005). Two fitting models were considered: the first one for ‘ideal’ octahedral $Zn(H_2O)_6$ aqueous complex, with Zn-O distances of 2.10 Å and the second for $ZnCl_4^{2-}$ species, with Zn-Cl of 2.20 Å (Mei et al. 2015). Theoretical backscattering amplitude and phase shift functions for Zn-O and Zn-Cl paths were calculated with the FEFF *ab initio* code (Mustre De Leon et al. 1991). For all compositions and *P*-*T* conditions, the fit parameters included the coordination number N_i, interatomic distances R_i, the mean-square relative displacement Debye-Waller factor σ^2_i, the energy shift ΔE_0, and the third cumulant c_3 which accounts for anharmonic disorder in the bond distances. The fits were performed simultaneously with *k*-weighting of 1, 2, and 3 so as to diminish correlations between N and σ^2 and R, ΔE_0, and c_3. The amplitude reduction factor $S0_2$ was fitted to 1.13 for the $[Zn(H_2O)_6]^{2+}$ aqueous ion at room conditions, assuming a fully hydrated Zn coordinated to six water molecules with Zn-O distance of 2.09 Å, and consequently set for all fits. ΔE_0 never exceeded 8 eV, further confirming the validity of the fitting procedure.

Results

Smithsonite solubility

Solubility results are reported in Table 2 and presented in Figure 3. Although the kinetics of the dissolution reactions was not investigated in this study, the similar solubility values (within experimental error) obtained with time lapse of ~30 minutes at the same *P*-*T* conditions suggest that thermodynamic equilibrium has been approached, if not attained.

From Figure 3 it can be seen that the solubility of smithsonite in water and NaCl aqueous solutions increases with increasing pressure and temperature. The highest measured total Zn concentration was 0.19(6) m at 5.0 GPa and 397 ˚C in the 1 m NaCl aqueous solution, about half an order of magnitude higher than the maximum solubility of 0.034 m previously reported at ~2 MPa, ~150 ˚C, and 5 m NaCl (Bourcier and Barnes 1987). These are, to the best of our knowledge, the first experimental constraints on smithsonite solubility in the GPa range.

The collection of solubility data following similar *P*-*T* paths in water, 1 and 4.5 m NaCl aqueous solutions allowed the evaluation of the effect of salinity (ionic strength). Over the pressure range studied (< 6 GPa) and for all investigated temperatures, smithsonite exhibits higher solubility in saline solutions than in pure water. The solubility decrease with increasing fluid salinity from 1 to 4.5 m (Figure 3) may be an artifact caused by the absorption of XRF signal by the matrix. The 4.5 m NaCl aqueous solution is significantly denser (1.13 gcm^{-3} compared to 1.03 gcm^{-3}) and has a much shorter absorption length at 8.6 keV (477 µm compared to 860 µm), although we note that the path length through the sample chamber is only of the order of tens of µm.

Solubility data collected along the 300 ˚C isotherms in the three fluids also allowed the quantification of the effect of pressure. In water, there is an approximately five-fold increase of solubility between 2.3 and 5.4 GPa. In 1 and 4.5 m NaCl aqueous solutions this increase is only approximately 30% between 2.1 and 5.9 GPa and between 2.5 and 5.9 GPa, respectively.

The effect of temperature could not be assessed independently of pressure. The change of mechanical properties of the DAC and the unavoidable change of pressure inside the DAC upon heating prevented us from following isobaric paths (e.g., Sanchez-

Valle et al. 2003; Louvel et al. 2014). A solubility increase was observed on heating from 300 to 400 ˚C in the 1 m NaCl aqueous solution. The increase in temperature was accompanied by a decrease in pressure from 5.9 to 5.0 GPa. The solubility increase is therefore inferred to be, principally, a temperature effect.

Fluid	Pressure (GPa)	Temperature (˚C)	Concentration (m)
H_2O	2.3	309	0.017(6)
	2.4	309	0.018(6)
	5.1	309	0.09(3)
	5.4	309	0.09(3)
	5.4	309	0.09(3)
1 m NaCl(aq)	2.1	294	0.14(2)
	5.3	294	0.19(6)
	5.2	294	0.19(6)
	5.3	294	0.19(6)
	5.9	295	0.19(6)
	5.9	295	0.19(6)
	5.0	397	0.18(5)
	5.0	397	0.18(5)
4.5 m NaCl(aq)	2.4	294	0.10(3)
	2.5	313	0.10(3)
	2.5	313	0.10(3)
	2.5	313	0.10(3)
	5.9	313	0.13(4)
	5.9	313	0.13(4)
	5.9	313	0.13(4)

Table 2. Solubility data for smithsonite. Concentration values are given as molality ($ZnCO_3$ dissolved per kg H_2O). The solubility decrease from the 1 to 4.5 m NaCl aqueous solution may be an artifact caused by the absorption of XRF signal by the matrix.

Zn complexation

Normalized Zn K-edge XANES spectra are given in Figure 4a and their first derivatives in Figure 4b. The transition from octahedral to tetrahedral coordination is characterized by a ~2eV shift of the edge to lower energies observed only in the 4 m Cl solution from 200 ˚C onward.

Previous studies used LCF to quantify the ratio of octahedral $[Zn(H_2O)_{6-n}Cl_n]^{2-n}$ (n = 0-4) to tetrahedral $[Zn(H_2O)_{4-n}Cl_n]^{2-n}$ (n = 1-4) complexes. Quantification of the concentration of complexes sharing the same geometry is challenging, because substitution of O (or H_2O) by Cl results in a relatively minor decrease of the white-line amplitude and width (Bazarkina et al. 2010). However, comparison of our high *P*-*T* spectra to the work of Mei et al. (2015) suggests that spectra collected at the lowest *P*-*T* conditions in the least saline solution (with a white line position of ~9668 eV) and at the highest *P*-*T* conditions in the most saline solution (with a white line at ~9665 eV) represent pure octahedral $[Zn(H_2O)_6]^{2+}$ and tetrahedral $[ZnCl_4]^{2-}$ endmembers, respectively (Figure 4). The proportions of each endmember as a function of pressure, temperature, and salinity was consequently estimated from LCF of the XANES spectra (Table 3 and Figure 5). Although the LCF employed here was based on a fully chlorinated $[ZnCl_4]^{2-}$ tetrahedral complex, the relative ratios of fitting components (hexagonal vs. tetrahedral) are here qualitative indicators of the Cl/O ratio in the Zn local environment and the presence of intermediate octahedral $[Zn(H_2O)_{6-n}Cl_n]^{2-n}$ (n = 1-2) or tetrahedral $[Zn(H_2O)_{4-n}Cl_n]^{2-n}$ (n = 3-4) complexes (Harris et al. 2003; Mei et al. 2015) cannot be ruled out.

Overall, the LCF analysis suggests that Zn speciation evolves with increasing pressure, temperature, and salinity too. At 25 ˚C, the gentle shift of the white line its first derivative toward lower energy (Figure 4) and LCF of XANES spectra (Figure 5) indicates that tetrahedral species already exist at ambient temperature in the 4 m Cl solution. Increasing temperature to 200 and 300 ˚C results in the progressive shift of the white line toward lower energy and a gradual increase of the proportion of tetrahedral species with salinity (ionic strength) (Figure 5). At 400 ˚C, only tetrahedral species are seen in the 4 m Cl solution (Figure 5).

Measurements taken at 200 ˚C in the 0.2 m solution at two different pressures (Figures 4 and 5) suggest higher coordination (and hence less Cl) with increasing pressure (and fluid density). The effect of pressure and solvent properties on Zn speciation and the extent of chlorination is also apparent when comparing our 4 m (40:1) Cl solution at 0.58 GPa and 25 ˚C, where Zn is mostly found in octahedral coordination to the analysis of 3.7 m (37:1) Cl solution at 0.06 GPa and 30 ˚C by Mei et al. (2015), where tetrahedral complexes were suggested to dominate.

Solution	Pressure (GPa)	Temperature (˚C)	E_0 (eV)	Relative ratios of LCF components		R-factor
				$Zn(H_2O)_6$	$ZnCl_4$	
Solution 1 (0.2 m Cl)	0.54	25	9664.4	1.00	0.00	N/A
	1.00	200	9663.5	0.55	0.45	0.008
	1.60	200	9663.8	0.78	0.22	0.007
	1.53	300	9663.4	0.62	0.38	0.012
Solution 2 (1 m Cl)	0.60	25	9664.4	0.94	0.06	0.002
	1.95	200	9663.4	0.71	0.29	0.003
Solution 3 (4 m Cl)	0.58	25	9664.0	0.84	0.16	0.003
	1.06	200	9662.6	0.23	0.77	0.008
	1.68	300	9662.4	0.18	0.82	0.008
	1.96	400	9662.2	0.00	1.00	N/A

Table 3. Linear combination fitting results of XANES spectra. The respective proportions of fitting components are qualitative indicators of the Cl/O ratio in the local environment.

EXAFS analysis enables refinement of the LCF XANES observations. At ambient conditions, Zn is found to be fully hydrated in all solutions, surrounded by approximately six oxygens located at an average distance of 2.077-2.085 Å (Table 4 and Figure 6). Upon increase to 200 ˚C and 1-2 GPa, the best fits are obtained for an octahedral structure involving four to five oxygens from water and 1.1-1.7 Cl atoms in both diluted (0.2 m Cl) and intermediate (1 m Cl) salinities. These chloride complexes remain stable up to 300 ˚C and 1.53 GPa in the diluted 0.2 m Cl solution. Unfortunately, the increase in noise in the data for the high-salinity 4 m Cl solution 3 hindered EXAFS analysis at high *P*-*T* conditions. However, following the detailed studies of Bazarkina et al. (2010) and Mei et al. (2015), the shifts and changes of XANES shape presented in Figure 4 can robustly be attributed to the formation of tetrahedral $ZnCl_4^{2-}$ complexes from 200 ˚C onward. These complexes are found stable to 400 ˚C and 2 GPa.

Solution	Pressure (GPa)	Temperature (˚C)	N_O	R_O (Å)	σ^2_O	c_3	N_{Cl}	R_{Cl} (Å)	σ^2_{Cl}	ΔE_0	χ^{red}	R-factor
Solution 1 (0.2 m Cl)	0.54	25	6.0(6)	2.077(8)	0.020(2)	0.0031(6)				7.88(63)	57	0.0308
	1.00	200	4.3(5)	2.06(1)	0.0156(20)	0.0050(5)	1.7(4)	2.236(40)	0.0147(60)	8.61(170)	48	0.0435
	1.53	300	4.4(5)	2.046(13)	0.0216(27)	0.0058(8)	1.5(5)	2.204(41)	fixed*	7.51(170)	28	0.0595
Solution 2 (1 m Cl)	0.60	25	6.3(4)	2.080(24)	0.0209(16)	0.0039(8)				6.52(75)	23	0.0273
	1.95	200	4.9(4)	2.057(20)	0.0208(17)	0.0042(4)	1.1(4)	2.251(35)	fixed*	8.52(58)	12	0.0329
Solution 3 (4 m Cl)	0.58	25	6.2(4)	2.085(20)	0.0208(15)	0.0041(4)				7.36(169)	24	0.0223

fixed* $\sigma^2Cl = \sigma^2O$

S02 = 1.13

Table 4. Fit parameters extracted from the EXAFS analysis of Zn- K-edge spectra acquired at various conditions as given. Parameters including the number of neighbours (*N*), the interatomic distances (*R*) and the mean-square relative displacement Debye-Waller factor σ^2 and the anharmonic contribution c_3 to the spectrum for oxygen and chlorine as next-nearest neighbour to the central absorbing Zn atom. Further the fitted energy shift (ΔE_0) and the fit quality parameters reduced chi (χ^{red}) and the R-factor are given.

Discussion

Effect of salinity, pressure, and temperature on smithsonite solubility and Zn aqueous behaviour

Our results demonstrate that Zn solubility of smithsonite increases with pressure and temperature. While increasing pressure leads to systematic solubility increase for most carbonate minerals (*e.g.*, calcite, aragonite, strontianite) irrespective of temperature conditions (Fein and Walther 1989; Caciagli and Manning 2003; Sanchez-Valle et al. 2003; Facq et al. 2014), the effect of temperature varies with pressure. At ambient pressure, increasing temperature results in the decrease of solubility of smithsonite (Egorov and Titova 1962; Helgeson 1969). A similar trend is observed for calcite up to 0.2 GPa (Segnit et al. 1962; Walther and Long 1986; Wolf et al. 1989). At higher pressure, however, the solubility trend with increasing temperature inverts and increases for calcite (Walther and Long 1986; Fein and Walther 1989; Newton and Manning 2002; Caciagli and Manning 2003). Our experiments underline a similar behaviour for smithsonite, for which increasing temperature only results in enhanced solubility at high pressures.

In parallel, while increasing salinity and temperature appear to favour the transition from octahedral O-coordinated to tetrahedral Cl-coordinated complexes (this work, Liu et al. 2007; Mei et al. 2015; Etschmann et al. 2019), our experiments suggest that increasing pressure inhibits this transition. First, in the experiment of Mei et al. (2015) tetrahedral complexes already prevail at 0.06 GPa and 30 ˚C in the solution with 3.7 m Cl_{tot}, while our data suggest that at 0.58 GPa and 25 ˚C in the solution with 4 m Cl_{tot}, octahedral complexes dominate (Figure 4). Second, increasing pressure from 1 to 1.6 GPa at 200 ˚C in the solution with 0.2 m Cl_{tot} results in the increase of octahedral complexes (Figure 5). It is likely that the tetrahedral $ZnCl_4$ - trigonal $ZnCl_3$ transition observed by Etschmann et al. (2019) in Cl-bearing solutions at 0.1 GPa and above 500 ˚C will also be inhibited by pressure. Given that the initial pH of our solutions is close to neutral, and the dissolution of relatively little $ZnCO_3$ does not change the pH significantly, the amount of other Zn species in our solutions (e.g., $Zn(OH)^+$, ZnO_2^{2-}) will be negligeable (Akinfiev and Tagirov 2014).

The *P-T* dependencies of smithsonite solubility are explained by changes in the properties of high *P-T* fluids with increasing *P-T* conditions and the formation of new Zn-Cl complexes as evidenced here. Solubility is indeed controlled by the relative dielectric permittivity of the solvent, ε, also known as dielectric constant (Weingärtner and Franck 2005). The high relative permittivity ($\varepsilon/\varepsilon_0$) of water (approximately 80) at near ambient conditions results from preferred dipole orientations in the water structure dominated by extended hydrogen bond network and is lowered to around 10-25 in the supercritical region (> 22 MPa and > 374 ˚C), where the hydrogen bond network is significantly disrupted (Weingärtner and Franck 2005). Increasing salinity leads to a further decrease of permittivity, a phenomenon termed dielectric decrement (Hasted et al. 1948). This explains the formation of $ZnCl_4^{2-}$ in the 4 m Cl solution, as the lower ε will favour ion association and lower coordination number for the dissolved ions. It appears that the formation of such complexes favours the dissolution of smithsonite in the high *P-T* fluids, as higher Zn concentrations are reported for the 4 m Cl solution than 0.2 m Cl solution. While we could not determine the speciation of Zn in the 1 m Cl solution 2 above 200 ˚C and 2 GPa, the high solubility of Zn (Figure 3) hints to the formation of tetrahedral $ZnCl_4^{2-}$ under these conditions. Thus, the transition from octahedral to tetrahedral Zn chloride complexes is expected to occur between 200 and 300 ˚C at pressures in the 1-2 GPa range.

Owing to the low dielectric permittivity in the saline supercritical fluid, pressure and temperature effects are more pronounced. Increasing pressure leads to higher fluid density, strengthening the hydrogen bond network, higher coordination of dissolved ions, their extensive hydration and decreased ion association (Sakuma and Ichiki 2016).

Our XAS results confirm the importance of this pressure effect, as octahedral hydrated chloride $[Zn(H_2O)_{6-n}Cl_n]^{2-n}$ (n = 1-2) complexes are found stable to 200-300 ˚C and 1.5-2 GPa in fluids containing 0.2-1 m Cl, when previous studies conducted at lower pressures (Mei et al. 2015; Etschmann et al. 2019) suggested the formation of tetrahedral $[Zn(H_2O)_{4-n}Cl_n]^{2-n}$ (n = 1-4) complexes at similar salinity and temperature conditions. In contrast to pressure effects, increasing temperature will lower the density of fluid, disrupt the hydrogen bond network, lower the coordination of dissolved ions and their hydration and enhance ion-ion interactions. The competing effects of pressure and temperature and their role in Zn speciation can be seen in Figure 5. The increase of solubility with increasing ionic strength can be explained by enhanced ion-ion (e. g., Zn–Cl) interactions.

Controls on Zn aqueous mobilization at subduction zones and isotopic signature of slab-derived fluids

Smithsonite is stable across a wide range of *P*-*T* conditions in both aqueous and anhydrous environments and therefore represents an important potential Zn reservoir in the crust and upper mantle (Haselton and Goldsmith 1987; Preis et al. 2000; Farsang et al. 2021). Upon slab dehydration, smithsonite and other Zn-bearing minerals (*e.g.*, sphalerite) are expected to dissolve in the released fluids. The dependencies of solubility on salinity (ionic strength) suggest that relatively high solubilities are expected in fluids with ionic strength around 1 m, which is a typical value for most crustal and slab-derived fluids (*e.g.*, Scambelluri and Philippot 2001; Seward et al. 2014 and references therein). The change of coordination from octahedral to tetrahedral further enhances the solubility of smithsonite in Cl-rich fluids and provides a likely mechanism for the efficient uptake of Zn by slab-derived fluids. The precipitation of most Zn-bearing phases likely happens in regions with high temperature gradient, where the largest change in solubility is expected. The solubility of smithsonite is likely to increase dramatically as it approaches its melting temperature (not yet constrained at the conditions of this study, but expected to take place at temperatures lower than those of slab melting) as seen in the case of calcite (Newton and Manning 2002).

Our experiments are limited to Cl-rich environments. However, it is important to recognise the chemical heterogeneity of subduction zones and associated slab-derived fluid compositions and the presence of other, potentially important transporting agents. In S-rich settings, Zn may be preferentially transported either as bisulfide or sulphate complexes (*e.g.*, Mei et al. 2016; Etschmann et al. 2019). Zn stable isotope systematics may provide a means to distinguish between these scenarios and identify the predominant Zn transporting complex in slab-derived fluid (Pons et al. 2016). Fujii et al. (2011, 2014) used Density Functional Theory (DFT) calculations to derive reduced partition function ratios for Zn and different ligands (*e.g.,* $[Zn(H_2O)_6]^{2+}$, $[ZnCl_4]^{2-}$, $[Zn(HS)_4]^{2-}$, $ZnSO_4(H_2O)_5$, $ZnCO_3(H_2O)_3$). Pons et al. (2016) used these data to model the $\delta^{66}Zn$ evolution of released fluids (and residual serpentinites), as a function of the prevalent Zn carrying ligands. Accordingly, they attributed distinct $\delta^{66}Zn$ values of rocks (ranging from 0.32±0.08 ‰ in oceanic lizardite-serpentinites to 0.17±0.08 ‰ in antigorite-serpentinites) along with additional petrologic evidence (*e.g.,* sulphur concentration) to the presence of high amounts of SO_4^{2-} in the slab-derived fluids from the Alpine subduction settings of their study. Whereas this model assumed $ZnCl(H_2O)_5$ is the dominant Cl-bearing complex, our data and previous XAS studies (Liu et al. 2007; Mei et al. 2015; Etschmann et al. 2019) suggest that this complex may be irrelevant at the high *P-T* conditions, salinities, and pH conditions of subduction zone fluids, where $[ZnCl_4]^{2-}$ or $[ZnCl_3]^-$ are more likely to prevail. A further complication may arise from the role of pressure. The theoretical DFT calculations of isotope fractionation were performed for ambient pressure, and applied to high pressures, whereas it is known that pressures in the GPa range may have considerable direct or indirect effects on isotope fractionation (Gillet et al. 1996; Polyakov 1998). A potentially important indirect consequence may be the formation of a highly ionic supercritical fluid with physical and chemical properties very different to those of water at ambient conditions (Weingärtner and Franck 2005). In future geochemical modelling, the implementation of high *P*-*T* speciation data as well as the use of isotope fractionation factors taking pressure effects into account is recommended.

Conclusions

We have studied the effect of increasing salinity (0-4.5 m total Cl), pressure and temperature on the solubility of smithsonite ($ZnCO_3$) and speciation of Zn in aqueous fluids up to 6 GPa and 400 ˚C. The solubility of smithsonite increases with both pressure and temperature (over the range of conditions of our study) and reaches wt% level solubilities in NaCl aqueous solutions, implying high solubilities in crustal and slab-derived fluids. In agreement with previous studies conducted at lower pressures (below 1 GPa), we observe a gradual transition from octahedral hydrated $[Zn(H_2O)_6]^{2+}$ to tetrahedral hydrated and chlorinated $[Zn(H_2O)_{4-n}Cl_n]^{2-n}$ (n = 1-4) complexes with increasing salinity and temperature (Liu et al. 2007; Mei et al. 2015; Etschmann et al. 2019). The tetrahedral complexes remain stable under conditions relevant to cold slab dehydration. Pressure drives the reverse effect on speciation and appears to hinder the octahedral to tetrahedral transition. Pressure clearly has an important effect on Zn coordination, and speciation models as well as extrapolation algorithms should take this into account. The role of S in Zn transport at pressures in the GPa range remains uncertain and further high-pressure experiments focusing on the solubility and complexation at temperatures exceeding 400 ˚C in Cl- and S-rich fluids should therefore be conducted.

Acknowledgements

Robin Hansen and Michael S. Rumsey of the Natural History Museum, London, UK are acknowledged for the smithsonite sample. Giulio I. Lampronti, Iris Buisman, and Jason Day are acknowledged for their assistance with XRD, EPMA, and ICPMS analysis, respectively. ESRF is acknowledged for access to beamline BM23 (ES-791) and DLS for access to beamline I20-EDE (SP21869). We also gratefully acknowledge the BM23 team, including Olivier Mathon, Sébastien Pasternak, and Florian Perrin for technical assistance and implementation of the new setup and Jeroen Jacobs and Harald Mueller for their technical assistance. We are very grateful to Elena F. Bazarkina for her helpful comments and insightful review of this paper. This work was supported by the Natural Environment Research Council (grant number NE/L002507/1).

References

Akinfiev, N.N., and Tagirov, B.R. (2014) Zn in hydrothermal systems: Thermodynamic description of hydroxide, chloride, and hydrosulfide complexes. Geochemistry International, 52, 197–214.

Bassett, W.A., Anderson, A.J., Mayanovic, R.A., and Chou, I.-M. (2000) Hydrothermal diamond anvil cell for XAFS studies of first-row transition elements in aqueous solutions up to supercritical conditions. Chemical Geology, 167, 3–10.

Bazarkina, E.F., Pokrovski, G.S., Zotov, A. V, and Hazemann, J. (2010) Structure and stability of cadmium chloride complexes in hydrothermal fluids. Chemical Geology, 276, 1–17.

Bourcier, W.L., and Barnes, H.L. (1987) Ore solution chemistry-VII. Stabilities of chloride and bisulfide complexes of zinc to 350°C. Economic Geology, 82, 1839–1863.

Caciagli, N.C., and Manning, C.E. (2003) The solubility of calcite in water at 6-16 kbar and 500-800 °C. Contributions to Mineralogy and Petrology, 146, 275–285.

Clever, H.L., Derrick, M.E., and Johnson, S.A. (1992) The solubility of some sparingly soluble salts of zinc and cadmium in water and in aqueous electrolyte solutions. Journal of Physical and Chemical Reference Data, 21, 941–966.

Dewaele, A., Svitlyk, V., Bottin, F., Bouchet, J., and Jacobs, J. (2018) Iron under conditions close to the $\alpha - \gamma - \epsilon$ triple point. Applied Physics Letters, 112, 1–5.

Diaz-Moreno, S., Amboage, M., Basham, M., Boada, R., Bricknell, N.E., Cibin, G., Cobb, T.M., Filik, J., Freeman, A., Geraki, K., and others (2018) The Spectroscopy Village at Diamond Light Source. Journal of Synchrotron Radiation, 25, 998–1009.

Egorov, A.M., and Titova, Z.P. (1962) Temperature dependence of solubility products of salts with polyatomic ions. Russian Journal of Inorganic Chemistry, 7, 141–142.

Etschmann, B., Liu, W., Mayanovic, R., Mei, Y., Heald, S., Gordon, R., and Brugger, J. (2019) Zinc transport in hydrothermal fluids: On the roles of pressure and sulfur vs. chlorine complexing. American Mineralogist, 104, 158–161.

Facq, S., Daniel, I., Montagnac, G., Cardon, H., and Sverjensky, D.A. (2014) In situ Raman study and thermodynamic model of aqueous carbonate speciation in equilibrium with aragonite under subduction zone conditions. Geochimica et Cosmochimica Acta, 132, 375–390.

Farsang, S., Widmer, R.N., and Redfern, S.A.T. (2021) High-pressure and high-temperature vibrational properties and anharmonicity of carbonate minerals up to 6 GPa and 500 °C by Raman spectroscopy. American Mineralogist, 106, 581–598.

Fei, Y., Ricolleau, A., Frank, M., Mibe, K., Shen, G., and Prakapenka, V. (2007) Toward an internally consistent pressure scale. Proceedings of the National Academy of Sciences, 104, 9182–9186.

Fein, J.B., and Walther, J. V. (1989) Calcite solubility and speciation in supercritical NaCl-HCl aqueous fluids. Contributions to Mineralogy and Petrology, 103, 317–324.

Fujii, T., Moznier, F., Pons, M.-L., and Albaréde, F. (2011) The origin of Zn isotope fractionation in sulfides. Geochimica et Cosmochimica Acta, 75, 7632–7643.

Fujii, T., Moynier, F., Blichert-Toft, J., and Albarède, F. (2014) Density functional theory estimation of isotope fractionation of Fe, Ni, Cu, and Zn among species relevant to geochemical and biological environments. Geochimica et Cosmochimica Acta, 140, 553–576.

Gao, J., Zhu, F., Lai, X.-J., Huang, R., Qin, S., Chen, D.-L., Liu, J., Zheng, L.-R., and Wu, X. (2014) Compressibility of a natural smithsonite $ZnCO_3$ up to 50 GPa. High Pressure Research, 34, 89–99.

Gillet, P., Mcmillan, P., Schott, J., Badro, J., and Grzechnik, A. (1996) Thermodynamic properties and isotopic fractionation of calcite from vibrational spectroscopy of ^{18}O-substituted calcite. Geochimica et Cosmochimica Acta, 60, 3471–3485.

Harris, D.J., Brodholt, J.P., and Sherman, D.M. (2003) Zinc complexation in hydrothermal chloride brines: Results from ab initio molecular dynamics calculations. Journal of Physical Chemistry A, 107, 1050–1054.

Haselton, H.T., and Goldsmith, J.R. (1987) The decarbonation and heat capacity of $ZnCO_3$. Geochimica et Cosmochimica Acta, 51, 261–265.

Hasted, J.B., Ritson, D.M., and Collie, C.H. (1948) Dielectric properties of aqueous ionic solutions. Parts I and II. The Journal of Chemical Physics, 16, 1–21.

Helgeson, H.C. (1969) Thermodynamics of hydrothermal systems at elevated temperatures and pressures. American Journal of Science, 267, 729–804.

Letoullec, R., Pinceaux, J.P., and Loubeyre, P. (1988) The membrane diamond anvil cell: A new device for generating continuous pressure and temperature variations. High Pressure Research, 1, 77–90.

Liu, S.-A., Wang, Z.-Z., Li, S.-G., Huang, J., and Yang, W. (2016) Zinc isotope evidence for a large-scale carbonated mantle beneath eastern China. Earth and Planetary Science Letters, 444, 169–178.

Liu, W., Etschmann, B., Foran, G., Shelley, M., and Brugger, J. (2007) Deriving formation constants for aqueous metal complexes from XANES spectra: Zn^{2+} and Fe^{2+} chloride complexes in hypersaline solutions. American Mineralogist, 92, 761–770.

Louvel, M., Sanchez-Valle, C., Malfait, W.J., Testemale, D., and Hazemann, J.L. (2013) Zr complexation in high pressure fluids and silicate melts and implications for the mobilization of HFSE in subduction zones. Geochimica et Cosmochimica Acta, 104, 281–299.

Louvel, M., Sanchez-Valle, C., Malfait, W.J., Cardon, H., Testemale, D., and Hazemann, J.-L. (2014) Constraints on the mobilization of Zr in magmatic-hydrothermal processes in subduction zones from in situ fluid-melt partitioning experiments. American Mineralogist, 99, 1616–1625.

Louvel, M., Drewitt, J.W.E., Ross, A., Thwaites, R., Heinen, B.J., Keeble, D.S., Beavers, C.M., Walter, M.J., and Anzellini, S. (2020) The HXD95: a modified Bassett-type hydrothermal diamond-anvil cell for in situ XRD experiments up to 5 GPa and 1300 K. Journal of Synchrotron Radiation, 27, 1–9.

Mathon, O., Beteva, A., Borrel, J., Bugnazet, D., Gatla, S., Hino, R., Kantor, I., Mairs, T., Munoz, M., Pasternak, S., and others (2015) The time-resolved and extreme conditions XAS (TEXAS) facility at the European Synchrotron Radiation Facility: the general-purpose EXAFS bending-magnet beamline BM23. Journal of Synchrotron Radiation, 22, 1548–1554.

Mayanovic, R.A., Anderson, A.J., Bassett, W.A., and Chou, I.-M. (1999) XAFS measurements on zinc chloride aqueous solutions from ambient to supercritical conditions using the diamond anvil cell. Journal of Synchrotron Radiation, 6, 195–197.

Mei, Y., Sherman, D.M., Liu, W., Etschmann, B., Testemale, D., and Brugger, J. (2015) Zinc complexation in chloride-rich hydrothermal fluids (25-600 °C): A thermodynamic model derived from ab initio molecular dynamics. Geochimica et Cosmochimica Acta, 150, 265–284.

Mei, Y., Etschmann, B., Liu, W., Sherman, D.M., Testemale, D., and Brugger, J. (2016) Speciation and thermodynamic properties of zinc in sulfur-rich hydrothermal fluids: Insights from ab initio molecular dynamics simulations and X-ray absorption spectroscopy. Geochimica et Cosmochimica Acta, 179, 32–52.

Mustre De Leon, J., Rehr, J.J., Zabinsky, S.I., and Albers, R.C. (1991) Ab initio curved-wave x-ray-absorption fine structure. Physical Review B, 44, 4146–4156.

Newton, R.C., and Manning, C.E. (2002) Experimental determination of calcite solubility in H_2O-NaCl solutions at deep crust/upper mantle pressures and temperatures: Implications for metasomatic processes in shear zones. American Mineralogist, 87, 1401–1409.

Plyasunov, A. V, and Ivanov, I.P. (1991) The solubility of zinc oxide in sodium chloride solutions up to 600 ˚C and 1000 bar. Geochemistry International, 28, 77–90.

Polyakov, V.B. (1998) On anharmonic and pressure corrections to the equilibrium isotopic constants for minerals. Geochimica et Cosmochimica Acta, 62, 3077–3085.

Pons, M.-L., Debret, B., Bouilhol, P., Delacour, A., and Williams, H. (2016) Zinc isotope evidence for sulfate-rich fluid transfer across subduction zones. Nature Communications, 7, 13794.

Preis, W., Königsberger, E., and Gamsjäger, H. (2000) Solid-solute phase equilibria in aqueous solution. XII. Solubility and thermal decomposition of smithsonite. Journal of Solution Chemistry, 29, 605–618.

Prescher, C., and Prakapenka, V.B. (2015) DIOPTAS: A program for reduction of two-dimensional X-ray diffraction data and data exploration. High Pressure Research, 35, 223–230.

Ravel, B., and Newville, M. (2005) ATHENA, ARTEMIS, HEPHAESTUS: data analysis for X-ray absorption spectroscopy using IFEFFIT. Journal of Synchrotron Radiation, 12, 537–541.

Ruaya, J.R., and Seward, T.M. (1986) The stability of chlorozinc(II) complexes in hydrothermal solutions up to 350°C. Geochimica et Cosmochimica Acta, 50, 651–661.

Sakuma, H., and Ichiki, M. (2016) Density and isothermal compressibility of supercritical H_2O-NaCl fluid: Molecular dynamics study from 673 to 2000 K, 0.2 to 2 GPa, and 0 to 22 wt% NaCl concentrations. Geofluids, 16, 89–102.

Sanchez-Valle, C., Martinez, I., Daniel, I., Philippot, P., Bohic, S., and Simionovici, A. (2003) Dissolution of strontianite at high P-T conditions: An in-situ synchrotron X-ray fluorescence study. American Mineralogist, 88, 978–985.

Scambelluri, M., and Philippot, P. (2001) Deep fluids in subduction zones. Lithos, 55, 213–227.

Schmidt, C., Steele-MacInnis, M., Watenphul, A., and Wilke, M. (2013) Calibration of zircon as a Raman spectroscopic pressure sensor to high temperatures and application to water-silicate melt systems. American Mineralogist, 98, 643–650.

Segnit, E.R., Holland, H.D., and Biscardi, C.J. (1962) The solubility of calcite in aqueous solutions-I The solubility of calcite in water between 75° and 200° at CO_2 pressures up to 60 atm. Geochimica et Cosmochimica Acta, 26, 1301–1331.

Seward, T.M., Williams-Jones, A.E., and Migdisov, A.A. (2014) The chemistry of metal transport and deposition by ore-forming hydrothermal fluids, 2nd ed., 29–57 p. Treatise on Geochemistry: Second Edition. Elsevier Ltd.

USGS (2020) Mineral commodity summaries 2020, 200 p. Reston, VA.

Walther, J. V, and Long, M.I. (1986) Experimental determination of calcite solubilities in supercritical H_2O. In Int Symp Water-Rock Interaction Vol. 5, pp. 609–611.

Weingärtner, H., and Franck, E.U. (2005) Supercritical water as a solvent. Angewandte Chemie - International Edition, 44, 2672–2692.

Weiss, Y., McNeill, J., Pearson, D.G., Nowell, G.M., and Ottley, C.J. (2015) Highly saline fluids from a subducting slab as the source for fluid-rich diamonds. Nature, 524, 339–342.

Wilke, M., Appel, K., Vincze, L., Schmidt, C., Borchert, M., and Pascarelli, S. (2010) A confocal set-up for micro-XRF and XAFS experiments using diamond-anvil cells. Journal of Synchrotron Radiation, 17, 669–675.

Wolf, M., Breitkopf, O., and Puk, R. (1989) Solubility of calcite in different electrolytes at temperatures between 10° and 60°C and at CO_2 partial pressures of about 1 kPa. Chemical Geology, 76, 291–301.

List of figures

Figure 1 a) Schematic diagram and image of the experimental setup at the BM23 beamline of ESRF. b) Close-up image of the vacuum box and the membrane diamond anvil cell. c) Schematic diagram and picture of the experimental setup at the I20-EDE beamline of DLS. d) Close-up image of the hydrothermal diamond anvil cell.

Figure 2 Pressure and temperature conditions of the X-ray fluorescence (XRF) spectroscopy and X-ray absorption spectroscopy (XAS) measurements.

Figure 3 Solubility of smithsonite as a function of pressure and temperature (indicated in ˚C next to data points) in aqueous solutions of different ionic strength. Note the log scale. The solubility decrease from the 1 to 4.5 m NaCl aqueous solution may be an artifact caused by the absorption of XRF signal by the matrix.

Figure 4 a) Normalized Zn K-edge XANES spectra and b) first derivative of the normalized Zn K-edge XANES spectra, as a function of salinity, pressure, and temperature. The shift to lower energies with increasing temperature in the 4 m solution indicates a transition from octahedral to tetrahedral hydrated Zn complexes.

Figure 5 Linear combination fitting of XANES spectra. Routes of different colours correspond to individual experimental runs and points along them indicate speciation at given pressure and temperature. The vertical segment of the grey route corresponds to isothermal pressurization. The numbers next to data points indicate pressure in GPa.

Figure 6 EXAFS spectra recorded during individual experimental runs as a function of salinity, pressure, and temperature. Dashed lines underline the transition from octahedral to tetrahedral hydrated Zn complexes.

Supplementary material

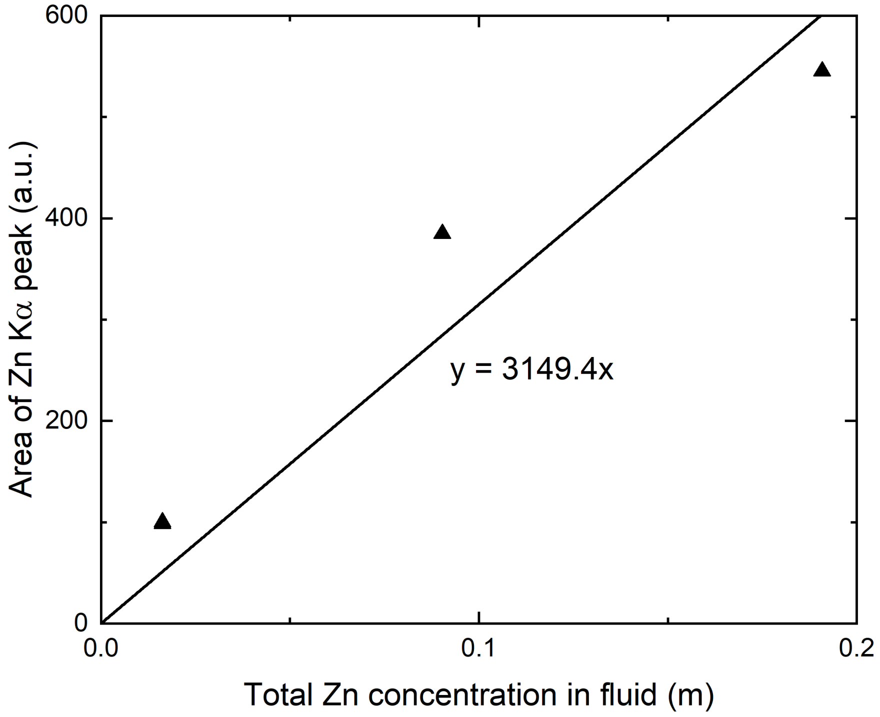

Figure S1 Variation of the Zn Kα fluorescence peak area in standard ZnCl$_2$ reference solutions. Black triangles represent measured values and the solid line presents the calibration curve fitted to the data points which was used for the latter analysis.

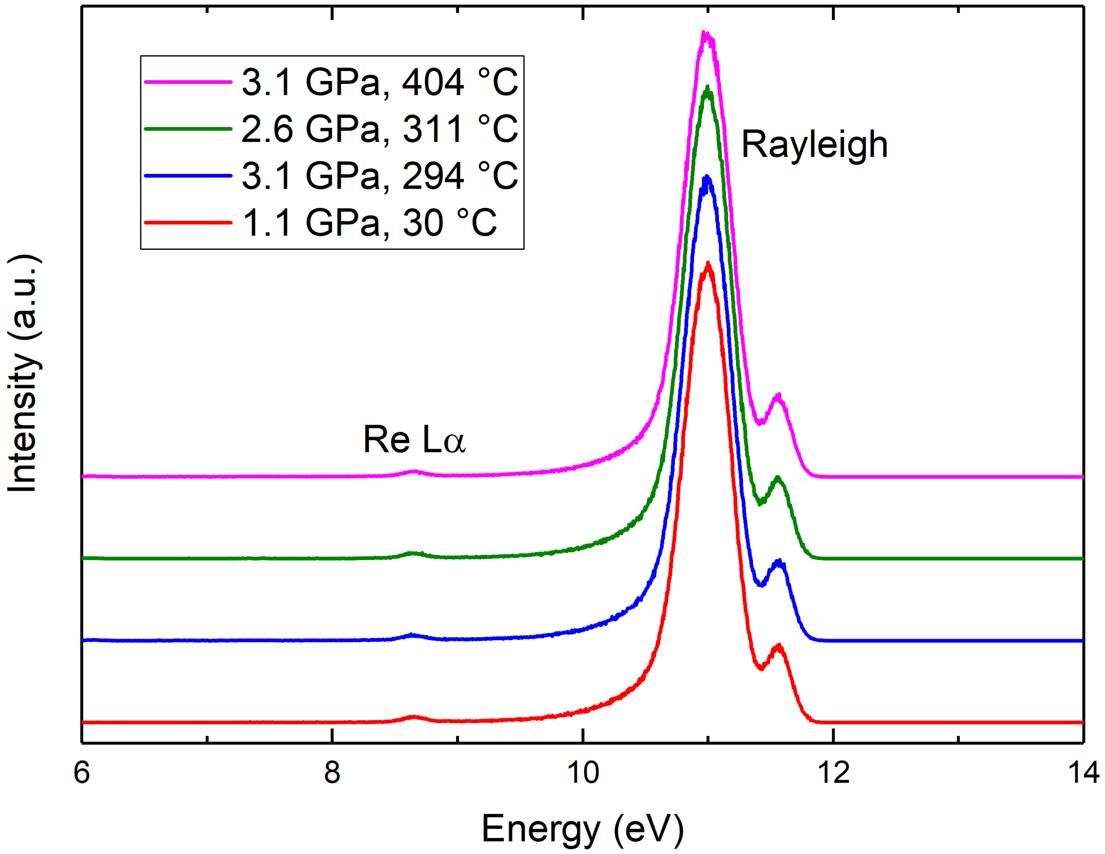

Figure S2 Synchrotron fluorescence spectra of the 1m NaCl aqueous solution collected at different *P*-*T* conditions for the blank experiment with no smithsonite crystal loaded in the DAC. The Re Lα peak remains weak and of constant magnitude across the range of *P*-*T* conditions of our experiments.